21

Advanced Numerical Simulation of Organic Light-emitting Devices

Beat Ruhstaller[1], Evelyne Knapp[2], Benjamin Perucco[3], Nils Reinke[4], Daniele Rezzonico[5] and Felix Müller[6]
[1,2,3,4]*Zurich University of Applied Sciences, Institute of Computational Physics, 8401 Winterthur*
[5,6]*Fluxim AG, 8835 Feusisberg*
Switzerland

1. Introduction

Organic light-emitting devices (OLEDs) are novel and efficient light sources that consist of a sequence of layers that fulfill distinct electronic and optical tasks. Given the variety of organic semiconductor materials available, the improvement of the device performance is a tedious and demanding task that often involves numerous experimental optimizations of layer materials, thicknesses and sequence. Comprehensive numerical device models have recently been developed that master both the physical complexity of the underlying optoelectronic processes as well as the numerically challenging system of equations. In this chapter we introduce such a comprehensive optical and electronic device model that is able to describe the device performance of OLEDs. We first introduce the key device model equations for charge and exciton transport as well as the dipole emission model for describing the out-coupling of light. Then we present a series of simulation results that are of practical interest when studying and optimizing OLEDs. These include the calculation of current-voltage curves, current transients signals, time-of-flight current transients and impedance spectroscopy data. We show that the physical model can be combined with a nonlinear least-square fitting algorithm for extracting transport parameters from measurements. In terms of optical device characteristics, quantitative outcoupling mode contributions and angular characteristics are presented as well as results of an emission zone extraction method.

Electrical characterization of devices and materials is essential and helps to elucidate the underlying, physical models of charge carrier transport in disordered, organic semiconductors. Besides the commonly used current-voltage curves, dark-injection, electroluminescence and time-of-flight transient measurements as well as impedance spectroscopy offer other ways to validate models for organic LEDs and extract model parameters. By means of a one-dimensional numerical OLED model we are able to simulate these different measurement techniques. Here, we present numerical methods in the physical and numerical framework of reference (Knapp et al, 2010) and solve directly for the steady- and transient state. Further, we conduct a numerical small signal-analysis for OLEDs. The underlying model solves the drift-diffusion equations in a coupled manner for disordered,

organic semiconductors. The disordered nature of organic semiconductors affects the density of state, the mobility model, the Einstein diffusion relation as well as charge injection. These novel physical model ingredients constitute a second generation OLED model and are implemented in the simulator SETFOS (Fluxim AG, 2010). It is expected that the second generation OLED model will impact the way OLED characteristics and performance are quantitatively described.

2. Description of the device model

2.1 Charge drift-diffusion model

To describe the main features of charge transport in organic LEDs four processes have to be considered as illustrated in the schematic energy level diagram in Fig. 1. In a first step, charge carriers have to be injected into the organic material (1), secondly they will be transported (2) until they recombine to an exciton (3). Then the excitons decay radiatively or non-radiatively (4). In the following we will first look at the transport process (2). For the description of

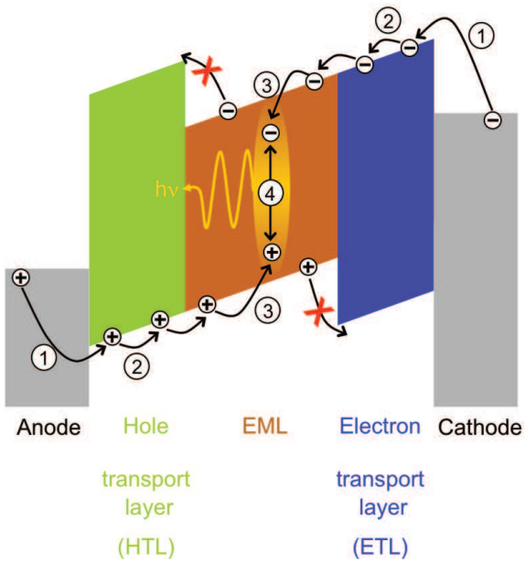

Fig. 1. Main processes in OLED operation: 1) Injection, 2) Transport, 3) Formation of exctions, 4) Radiative decay

charge transport in OLEDs the general semiconductor drift-diffusion equations for electrons and holes are valid. In Poisson's equation

$$\nabla \cdot (\epsilon \nabla \psi) = e(n + n_t - p - p_t), \tag{1}$$

the electrical potential ψ is related to the mobile electron and hole densities n and p and the trapped electron and hole densities n_t and p_t where e is the elementary charge and ϵ the product of the vacuum permittivity ϵ_0 and the relative permittivity ϵ_r of the organic material. The current equations for electrons and holes read

$$\begin{aligned} J_n &= -en\mu_n \nabla \psi + eD_n \nabla n, \\ J_p &= -ep\mu_p \nabla \psi - eD_p \nabla p \end{aligned} \tag{2}$$

where $\mu_{n,p}$ denotes the mobility and $D_{n,p}$ the diffusion coefficient for electrons and holes. Only mobile charges contribute to the current. The conservation of charges leads to the continuity equations for electrons and holes

$$\begin{aligned} \frac{\partial n}{\partial t} &= \frac{1}{e}\nabla J_n - R(n,p) - \frac{\partial n_t}{\partial t}, \\ \frac{\partial p}{\partial t} &= -\frac{1}{e}\nabla J_p - R(n,p) - \frac{\partial p_t}{\partial t} \end{aligned} \tag{3}$$

where R denotes the bimolecular recombination rate given by Langevin and t the time (Langevin, 1903). These equations take charge migration and recombination into account. The trapped electron (n_t) and hole (p_t) charge carriers obey the rate equations for an energetically sharp trap levels as shown in Fig. 2

$$\begin{aligned} \frac{\partial n_t}{\partial t} &= r_c n(N_t - n_t) - r_e n_t, \\ \frac{\partial p_t}{\partial t} &= r_c p(N_t - p_t) - r_e p_t. \end{aligned} \tag{4}$$

where r_e denotes the escape rate, r_c the capture rate and N_t the trap density. Note, that more general trap distributions can be introduced that are described by an exponential or Gaussian density of trap states (Fluxim AG, 2010; Knapp et al, 2010).

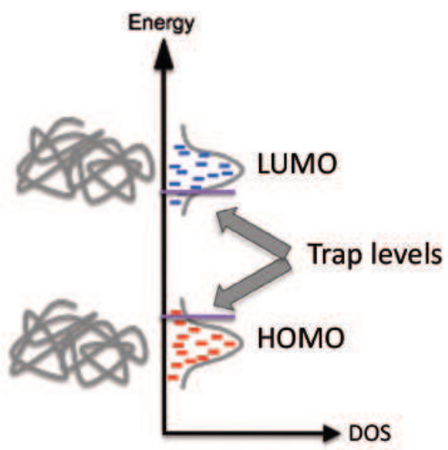

Fig. 2. Gaussian distributions of density of states and trap levels for trapped charges.

As opposed to inorganic semiconductors the density of states for organic semiconductors is described by a Gaussian shape since transport is assumed to occur via a hopping process between uncorrelated sites. Thus, polymers and small molecules have broadened energy levels of their highest occupied molecular orbital (HOMO) and lowest unoccupied molecular orbital (LUMO) as shown in Fig. 2 and are described in the following way

$$N_{Gauss}(E) = \frac{N_0}{\sqrt{2\pi\sigma^2}} \exp\left[-\left(\frac{E - E_0}{\sqrt{2}\sigma} \right)^2 \right] \tag{5}$$

where N_0 denotes the site density, σ the width of Gaussian and E_0 the reference energy level. In the extended Gaussian disorder model the Gaussian density of states affects charge diffusion. Tessler pointed out that the use of the generalized instead of the classical Einstein

relation is appropriate (Tessler et al., 2002). The generalized Einstein diffusion coefficient is now determined by

$$D = \frac{kT}{q}\mu(T,p,F)g_3(p,T), \tag{6}$$

where the enhancement function g_3 reads

$$g_3(p,T) = \frac{1}{kT}\frac{p}{\frac{\partial p}{\partial E_f}}. \tag{7}$$

Using the expression

$$p(E_f) = \int_{-\infty}^{\infty} DOS(E)f(E,E_f)dE \tag{8}$$

for the density and inserting the Fermi-Dirac distribution and the Gaussian DOS we obtain

$$\frac{D}{\mu} = \frac{kT}{q}\frac{\int_{-\infty}^{\infty} N_{Gauss}(E)\frac{1}{1+\exp\left(\frac{E-E_f}{kT}\right)}dE}{\int_{-\infty}^{\infty}\frac{N_{Gauss}(E)\exp\left(\frac{E-E_f}{kT}\right)}{[1+\exp\left(\frac{E-E_f}{kT}\right)]^2}dE}. \tag{9}$$

We will now turn to the charge mobility model. A mobility model that has been applied for quite some time now is the Poole-Frenkel mobility which is field-dependent and reads

$$\mu = \mu_0 \exp\left(\gamma\sqrt{E}\right), \tag{10}$$

where μ_0 is the zero-field mobility and γ is the field-dependence parameter. However, it has been shown by Bässler with the aid of Monte Carlo simulations that the energetic disorder in organic semiconductors influences the charge mobility (Pautmeier et al., 1990). Experiments have shown that the mobility in hole-only devices can differ up to three orders of magnitude between OLED and OFET device configurations with the same organic semiconductor. An explanation for this difference is a strong dependence of the mobility on the charge density (Tanase et al., 2003). Vissenberg and Matters developed a mobility model that considers such a density-dependent effect (Vissenberg & Matters, 1998). Using a 3D master equation approach to simulate the hopping transport in disordered semiconductors a dependence on the temperature, field and density was determined. Pasveer's model is therefore dependent on the temperature, field as well as the density and accounts for the disorder in the material (Pasveer et al, 2005). The extended Gaussian disorder model (EGDM) is an extension of the Pasveer model by additionally considering diffusion effects. In the EGDM the mobility may be expressed as a product of a density-dependent and field-dependent factor according to van Mensfoort as (Mensfoort et al., 2008a)

$$\mu(T,p,F) = \mu_0(T)g_1(p,T)g_2(F,T), \tag{11}$$

with the enhancement functions $g_1(p,T)$ and $g_2(F,T)$ accounting for the influence of the charge density, the electric field and the energetic disorder. The functions $g_1(p,T)$ and $g_2(F,T)$ are nonlinear and strongly increase with higher disorder parameter (Mensfoort et al., 2008b). In the remainder of this text, we will use either the traditional mobility model (Equation 10) or the advanced density-dependent model (Equation 11).

2.2 Exciton generation, transport and decay

This section describes the generation, transport and decay of excitons in organic semiconductor layers of OLEDs and becomes relevant in bipolar devices. While electron-hole recombination may be locally confined, the resulting excitons can migrate with a characteristic diffusion constant before decaying radiatively or transferring their energy to other exciton species in the same layer. Thus, the rate equation for exciton species S_i contains a generation, a diffusion, transfer and (non-)radiative terms:

$$\frac{dS_i(z)}{dt} = G_i R(z) + \vec{\nabla}\vec{J}_{s_i}(z) - (k_{rad_i}(z) + k_{nonrad_i}) \cdot S_i(z) - k_{annihilation_i} \cdot S_i(z)^2 + \\ + \sum_{j=1}^{n_{exc}} (k_{ji} \cdot S_j(z) - k_{ij} \cdot S_i(z)) \tag{12}$$

In Eq. 12 G_i is the generation efficiency prefactor, $k_{rad_i}(z)$ the position-dependent radiative decay rate, k_{nonrad_i} the non-radiative decay rate and $k_{annihilation_i}$ an annihilation rate. For a comprehensive fully-coupled opto-electronic OLED model, the radiative decay rate is calculated with the dipole emission model (see section 2.3 below) and ref. (Fluxim AG, 2010). In a classical view the generation efficiency for singlet excitons is $G_i = 0.25$ while it would be $G_i = 0.75$ for triplet excitons. The exciton energy transfer term $-k_{ij} \cdot S_i$ shall be used to model energy transfer from exciton S_i to exciton species S_j. Such exciton energy transfer rates can be taken from the literature. Common energy transfer mechanisms are Förster and Dexter transfer (Dexter, 1953; Förster, 1948). Förster transfer is a long-range dipole-dipole interaction while Dexter transfer is a short-range electron-exchange interaction. Both mechanisms rely on the spectral overlap of the emission spectrum of the donating exciton species with the absorption spectrum of the accepting exciton species. Exciton transport happens by diffusion and is therefore mathematically described by

$$J_{s_i} = D_s \nabla S_i \tag{13}$$

where D_s denotes the exciton diffusion constant.

2.3 Optical dipole emission model

In this section we present a model for the dipole emission describing the radiative decay of excitons in planar multi-layer systems. This model accounts for the influence of layer interfaces on the radiative decay rate of fluorescent molecules and is based on a classical theory for the emission of an oscillating electrical dipole. The basic concept of this theory was derived by Sommerfeld to analyze electromagnetic radiaton close to a conductive surface and extended by Chance et al. (Chance et al, 1978) to model fluorescence emission in optical cavities.

The emission characteristic of a single molecule is similar to that of a Hertzian dipole. However, in an infinite medium consisting of isotropically oriented molecules, the emission from the multitude of molecules is homogeneous in all directions. If, on the contrary, the molecules are embedded in a thin layer, interference effects of electromagnetic waves reflected at layer interfaces dominate the emission characteristics.

The dipole emission model allows to quantitatively analyze the individual energy loss channels of excited molecules. These energy loss channels include radiative coupling to the far-field, modes guided inside the multilayer structure as well as absorption losses by the surrounding media. The model is based on the following assumptions:

(1) Each medium of the multilayer system is assumed to be isotropic and only characterized by its dielectric permittivity ϵ.

(2) The medium embedding the emissive dipole is considered to be loss-free (i.e. real dielectric permittivity ϵ)

(3) The interface planes are infinitely extended.

(4) The wavelength λ of the radiation as well as the distance between the emitter and the individual interfaces is large with respect to the spatial extensions of the dipole (point dipole approximation).

(5) The dipole is at least at $\lambda/50$ distance away from the regions with a complex permittivity ϵ.

(6) The materials of the multilayer stack are considered to be non-magnetic.

Despite these restrictions, this model is valid for a wide range of physical situations. The model considers the molecules as driven damped harmonic dipole oscillators. These oscillators are damped by the emission process and driven by electric field components reflected at dielectric interfaces. An illustration of an emitting dipole near an interface is given in Fig. 3. The dynamics of the oscillating dipole moment $\vec{p}$ is described by the differential

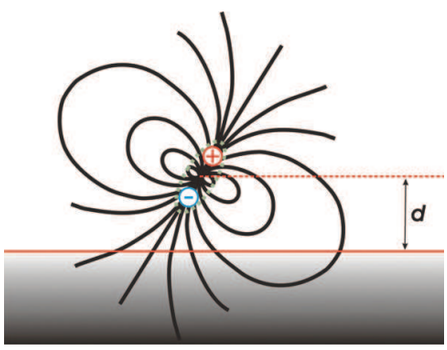

Fig. 3. Illustration of an emissive dipole near a reflecting interface at distance d.

equation

$$\frac{d^2}{dt^2}\vec{p} + b_0\frac{d\vec{p}}{dt} + \omega^2\vec{p} = \frac{e^2}{m}\vec{E}_R(\omega), \tag{14}$$

with the oscillator frequency ω, the elementary charge e, the effective mass m of the dipole, and $\vec{E}_R(\omega)$ the electric field at the dipole position. The radiative power of a dipole located inside an isotropic, infinite medium with a refractive index of n_e is

$$q_0 b_0 = \frac{|p|^2\omega k_0^3}{12\pi\epsilon_0} n_e,$$

where q_0 is the intrinsic quantum efficiency of the dipole and $k_0 = 2\pi/\lambda_0$. The intrinsic power of a dipole consists of a radiative and a non-radiative component.
The dynamics of a dipole located in an optical multilayer system is affected by the presence of the reflected field E_R and from its radiative character as

$$b = qb + (1-q)b, \tag{15}$$

where q is the modified quantum efficiency. The second term in Equation 15 refers to the *non-radiative* processes within the optical structure. These are not affected by the optical environment. Therefore we summarize the impact of the optical environment on the radiative part and write

$$b = q_0 b_0 \cdot F + (1 - q_0) b_0 \tag{16}$$

where F describes the influence of the electromagnetic field components on the oscillating dipole. F can be expressed by means of a generalized parametrization of the *emission* angle $u = \sin\theta_e$ as

$$F = \int_0^\infty f(u) du. \tag{17}$$

The total lifetime of a dipole in the optical system is consequently related to its intrinsic lifetime τ_0 by

$$\frac{\tau_0}{\tau} = \frac{b}{b_0} = (1 - q_0) + q_0 \cdot F. \tag{18}$$

Please note, that the above equations are modified for distinct dipole orientations and polarizations of the emitted light.

2.3.1 Mode Analysis

As seen above, the total dissipated power from the dipole is proportional to F and therefore, a stepwise integration of Equation 17 based on the index limits of total internal reflection allows to determine the fractional radiated power that can be assigned to out-coupled, guided (in the thin films), and evanescent modes. The integration limits are given by:

$$\begin{aligned} u &= 0 \ldots n_t/n_e && \text{radiative modes} \\ &= n_t/n_e \ldots 1 && \text{guided modes} \\ &= 1 \ldots \infty && \text{evanescent modes,} \end{aligned} \tag{19}$$

n_t and n_e being the refractive indices of the top and the emissive medium, respectively. The multilayer surrounding of the emitting dipole does not only affect its lifetime $\tau = \tau_0 \cdot b_0/b$, but also its radiative quantum efficiency. From Equation 15 and 16, the modified quantum efficiency q is therefore

$$q = \frac{q_0 \cdot F}{b/b_0}. \tag{20}$$

3. Simulation results

In this section, we present a number of simulation results that i) highlight the impact of energetic disorder on steady-state and transient currents as well as impedance spectra (subsections 3.1 to 3.3), ii) exemplify the fully-coupled electronic-optical simulation of multilayer OLEDs (subsection 3.4) and iii) demonstrate the use of time-of-flight transients under the influence of traps (subsection 3.5).

3.1 Steady-State Current-Voltage Curves

In the following we present the simulation results of a symmetric hole-only device under three different operating conditions. Thereby we consider the disordered nature of organic semiconductors that affects the density of states, the mobility model, the Einstein relation as well as charge injection. In this device the highest occupied molecular orbital (HOMO)

is aligned with the workfunctions of the anode and cathode. Therefore, we obtain a well-injecting anode and cathode. The high barrier for injection of electrons from the cathode to the lowest unoccupied molecular orbital (LUMO) level essentially leads to a hole-only device.
The high charge densities at the anode and cathode ($p(0)$ and $p(L)$) are set to half of the density of chargeable sites N_0, i.e. the Gaussian DOS is half-filled at either side due to the energy level alignment at the electrodes.

Parameter	Value	Units
N_0	$8.5 \cdot 10^{26}$	m^{-3}
σ	0.15	eV
μ_0	10^{-10}	$\mathrm{m}^2\mathrm{V}^{-1}\mathrm{s}^{-1}$
V_{bi}	0	V
$p(0)$	$0.5N_0$	m^{-3}
$p(L)$	$0.5N_0$	m^{-3}

Table 1. Simulation parameter set of the hole-only device for the three operating conditions.

First, we look at the best known electrical characterization method: the current-voltage curve. Therefore the steady-state for different voltages is calculated and we obtain current-voltage characteristics as shown in Fig. 4. We compare the steady-state results for the EGDM and the constant mobility case with the analytical solution which is given by

$$J(V) = \frac{9}{8}\varepsilon\varepsilon_0\mu_0\frac{V^2}{L^3} \tag{21}$$

where L denotes the length of the device, V the applied voltage and μ_0 the mobility (Mott & Gurney, 1938). All of the analytical solutions in the following are obtained by neglecting the diffusion and only taking the drift in Equation 2 into account. We observe the effect of diffusion especially at low voltages where the current is increased. In the regime of high bias the analytical solution and the constant mobility case merge whereas the EGDM solution moves away due to the field- and density-dependence of the EGDM and the slope of the EGDM curve is increased. Generally, the current density of the EGDM is higher due to the enhancement functions $g_1(p,T)$, $g_2(F,T)$ and $g_3(p,T)$. The EGDM has recently been successfully applied to current-voltage curves by van Mensfoort et al. (Mensfoort et al., 2008a). A comprehensive analysis of the effects of the EGDM and its components for the steady-state is conducted in reference (Mensfoort et al., 2008b).

3.2 Dark-injection transients

We now turn to the analysis of the time-dependent response to a step voltage. We perform transient simulations for the same device as above shown in Fig. 5. The dark-injection transients are simulated from 2 to 12 V in steps of 2 V. For the initial rise of the transient response the analytical solution is described by as

$$J(t) = \frac{2L\varepsilon\varepsilon_0}{\mu}\frac{1}{(2\tau_{SCF}-t)^2}, \tag{22}$$

where the space-charge-free transit time is defined as $\tau_{SCF} = \frac{L^2}{\mu V}$ (Helfrich & Mark, 1962). In the SCLC at the transit time $\tau_t = 0.786\tau_{SCF}$ the maximum current is obtained and reaches

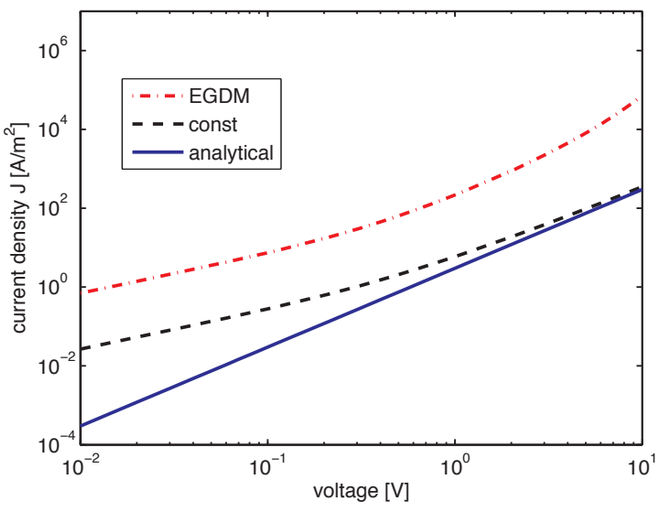

Fig. 4. Current-voltage curve for a hole-only device for a constant mobility and diffusion coefficient, the EGDM and the analytic solution (Mott-Gurney).

a value of $J(\tau_t) = 1.21 J_c$ where J_c stands for the stationary current from Mott-Gurney's law (Equation 21). The value of $J(\tau_t) = 1.21 J_c$ is marked in Fig. 5 with a star. Note that the slope of the line connecting these stars is minus two which can be explained with Equation 21. The relatively low charge mobility of organic semiconductors leads to space-charge limited transport. In this regime the transient response exhibits a cusp that relates to the transit time and thus the charge mobility. This has been the motivation for carrying out dark-injection transient experiments.

We notice that the peak position for the constant mobility case coincides well with the analytical solution, especially at high bias where the drift current is the dominant part of the total current. At low voltage the agreement becomes worse due to the diffusion current.

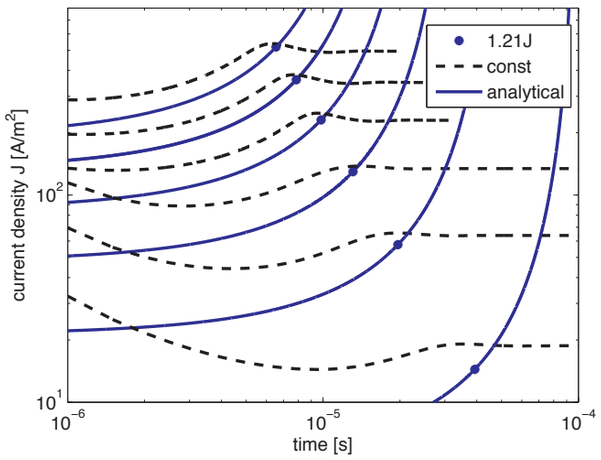

Fig. 5. Dark-injection transients for a hole-only device for a constant mobility and diffusion coefficient, the analytical solution and the generalized Einstein solution. The transients were simulated from 2 to 12 V.

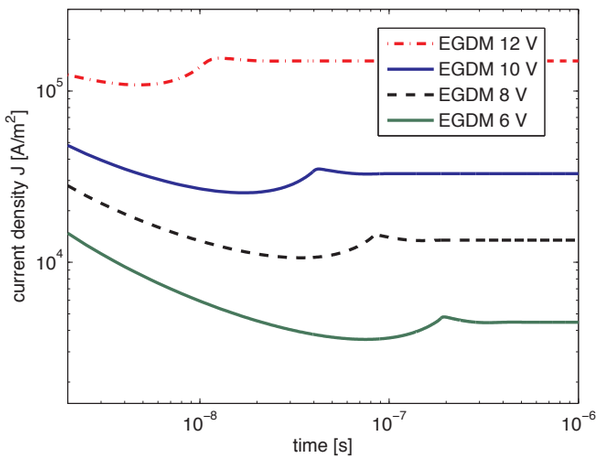

Fig. 6. Dark-injection transients for a hole-only device for the EGDM at different voltages.

If we also consider the enhancement functions for the EGDM as shown in Fig. 6, the peak positions shift to shorter times due to the enhanced mobility and the current density is vastly increased. In the EGDM case no formulas are available that would relate the peak position in the current with EGDM mobility parameters. Therefore, we have to rely on numerical fitting of the model parameters.

3.3 Impedance Analysis

As a third step, we investigate the response of the device to a voltage modulation. We obtain therefrom the impedance $Z(\omega)$ which is related to the admittance $Y(\omega)$ as

$$Y(\omega) = \frac{1}{Z(\omega)}. \tag{23}$$

The admittance is decomposed into an equivalent parallel conductance and capacitance as follows

$$Y(\omega) = G(\omega) + i\omega C(\omega). \tag{24}$$

We analyze the normalized capacitance at 8V in Fig. 7. We varied the energetic disorder parameter σ which is the main EGDM model parameter. We compare our numerical simulation results with the analytical solution for the drift-only case. For the small signal analysis the analytical solution for the impedance $Z(\omega)$ is given by

$$Z(\omega) = \frac{6}{g_0(i\omega\tau_0)^3}[1 - i\omega\tau_0 + \frac{1}{2}(i\omega\tau_0)^2 - \exp(-i\omega\tau_0)] \tag{25}$$

where $\tau_0 = \frac{4}{3}\frac{L^3}{\mu V}$ and $g_0 = \frac{3}{\tau_0}\frac{\epsilon}{L}$ (Shao & Wright, 1961). We also calculated the solution for the constant mobility case. The drift-only model provides a quite accurate solution for the constant mobility case at 8 V. At lower voltages however, the drift-only model differs significantly from the constant mobility model. We observe that the oscillations at high frequencies are damped out when diffusion is present. Also due to diffusion, the capacitance at low frequencies is increased from the typical value $\frac{3}{4}C_{geom}$ of the drift-only solution, even more in case of the EGDM. In the EGDM the peak position is additionally shifted to higher frequencies.

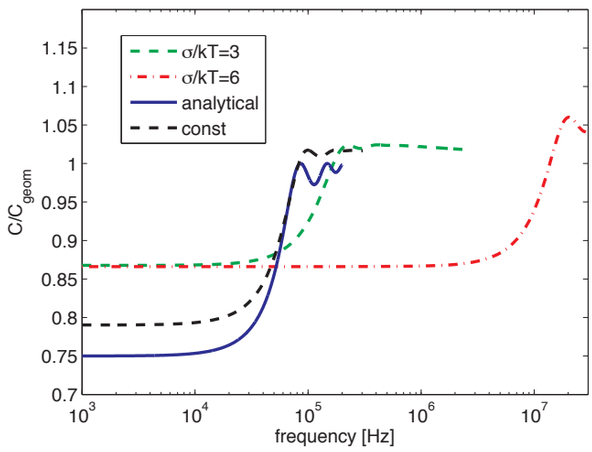

Fig. 7. Frequency dependence of the normalized capacitance at 6 V in a hole-only device for a constant mobility and diffusion coefficient, the EGDM and the analytical solution.

3.4 Fully-coupled electrical-optical OLED simulation

State-of-the art OLEDs are composed of several functional layers whose thickness obeys some optical or electronic criteria and which may be further complicated by dye doping, charge doping etc. The efficient harvesting of excitation energy by use of fluorescent and phosphorescent dye dopants remains a challenge. Here we attempt to give a simulation example of dual emitters in two layers EML1 and EML2 of a hypothetical 4-layer device structure. The rate equation for excitons (see Equation 12) is used here to model the energy transfer among different exciton species in a multilayer small-molecule OLED as depicted in Fig. 8.

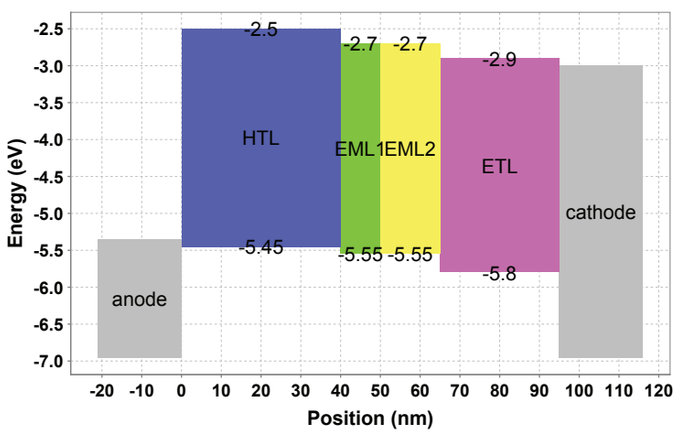

Fig. 8. Energy level diagram of a 4-layer OLED with two emissive layers EML1 and EML2 with two exciton species each.

The middle two layers were assumed to have emissive excitons in the host and guest material. The mobilities were assumed as illustrated in Fig. 10. The resulting charge distribution is shown in Fig. 9. For the chosen parameter values, the charges accumulate at either side of the EML2/ETL interface, thus also leading to a high electric field at that interface, see Fig. 9.
While only the excitons of the host materials EML1 and EML2 are excited by recombination events, the guest dye dopants receive their energy from the host by transfer. For this energy

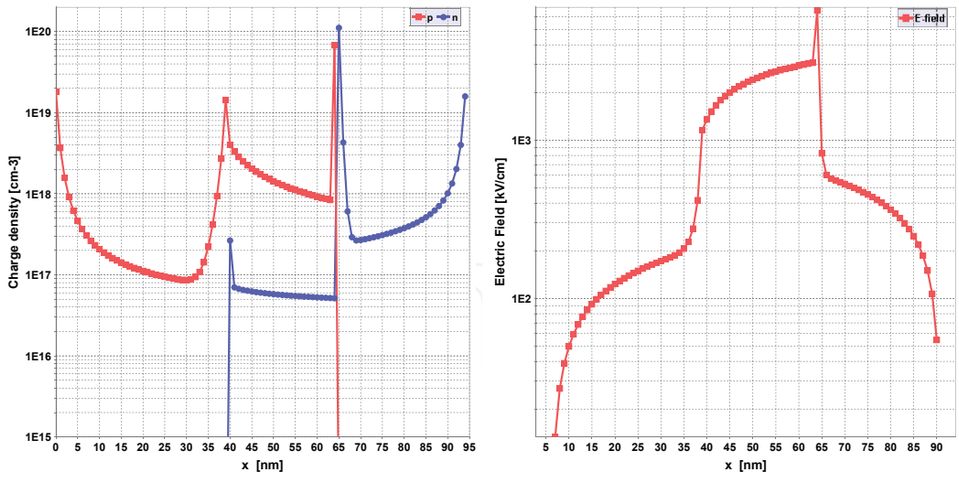

Fig. 9. Simulated profiles of charge carrier densities (left) and electric fields (right) for the hypothetical 4-layer OLED example of Fig. 8.

transfer we employ the transfer rate k_{ij} in Equation 12) and find that the guest excitons equilibriate in a different spatial distribution, due to a different parametrization, see Fig. 10 (right). The excitons are only modeled in the middle two layers.

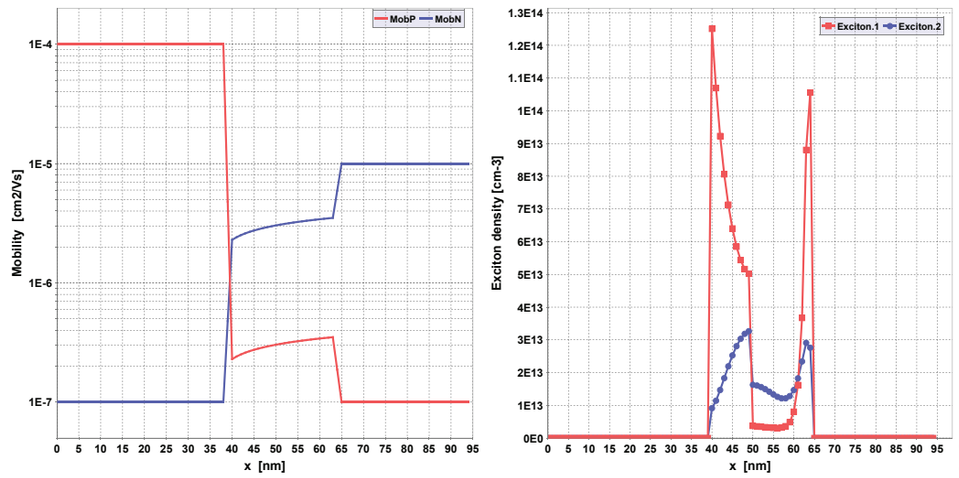

Fig. 10. Simulated profiles of mobilities (left) and Exciton.1 and Exciton.2 in the middle of the OLED structure (right).

If one is only interested in the steady-state, then the governing transport equations 3 are solved with an iterative steady-state solver (Fluxim AG, 2010; Knapp et al, 2010). However, if one is interested in the dynamics of charge transport, transient solution algorithms must be employed. Experimentally, the transient electroluminescence and transient current signals have revealed the dynamics of charge migration into the device (Ruhstaller et al., 2003; 2001). In Fig. 11 one can observe a monotonic increase of the recombination current, which testifies that the charges have first to penetrate the device before they can recombine. For the given hypothetical device, the charges are all consumed in the device, i.e. the recombination current is as large as the device current and therefore the current balance is equal to unity.

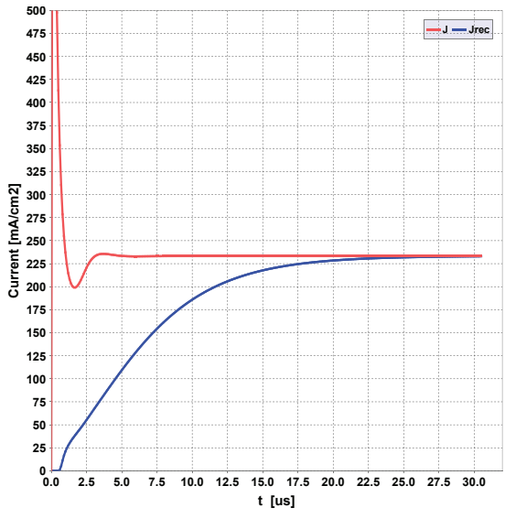

Fig. 11. Simulated device current and recombination current during turn-on.

This example simulation can be completed with a light-outcoupling calculation which takes the exciton distribution as dipole distribution. In this step one has to select which excitons are assumed to decay radiatively and thus contribute to light emission. For instance, we consider the emissive guest excitons in the emission layer EML1 and perform a calculation of the dissipated power versus the wavelength and the normalized in-plane wave vector u in Fig. 12 (left). The various emission modes can easily be identified qualitatively by looking at this plot. The guided modes are visible in the u range between 0.6 and 1. This power seems to exceed the power in the propagating outcoupled mode ($u < 0.6$) while the evanescent modes are displayed at values of u larger than 1. In addition in the left plot of Fig. 12 we report an analysis of emissive modes that takes care of the integration of the dissipated power of each mode in the relevant u ranges. The critical in-plane wavevector for light outcoupling into air is around 0.6 and the corresponding relative mode contribution is not more than 10%, in this example. Outcoupling efficiency numbers around 20% are typical values for OLEDs without any outcoupling enhancement techniques.

3.5 Numerical analysis of time-of-flight measurements

An exhaustive study of transport mechanisms in organic compounds shall comprehend the characterization of the charge dynamics. Time-of-flight (TOF) experiments are among the most common techniques to measure the mobility of the charges. Nevertheless, only a thorough analysis of the measured transient curves can give insight into the behavior of the charges, including the impact of trapped states. Current transients in TOF measurements are generally classified into dispersive and non-dispersive ones, the former being characterized by a monotonic decay of the measured current, while the latter show an initial plateau followed by a clear and sudden drop in the current.

In the following, we will investigate TOF transients by numerical simulations for distinct kinds of samples in order to allocate the specific characteristics of electron trap states. Here, we reproduce the TOF experiment presented by Malliaras et al. for Alq_3 devices that underwent different compound purification steps (Malliaras et al., 2001). The samples of our virtual experiment consisted of 8-μm Alq_3 films sandwiched between a transparent ITO layer and an aluminium (Al) electrode. The samples were reverse biased at a voltage of -1000 V, the

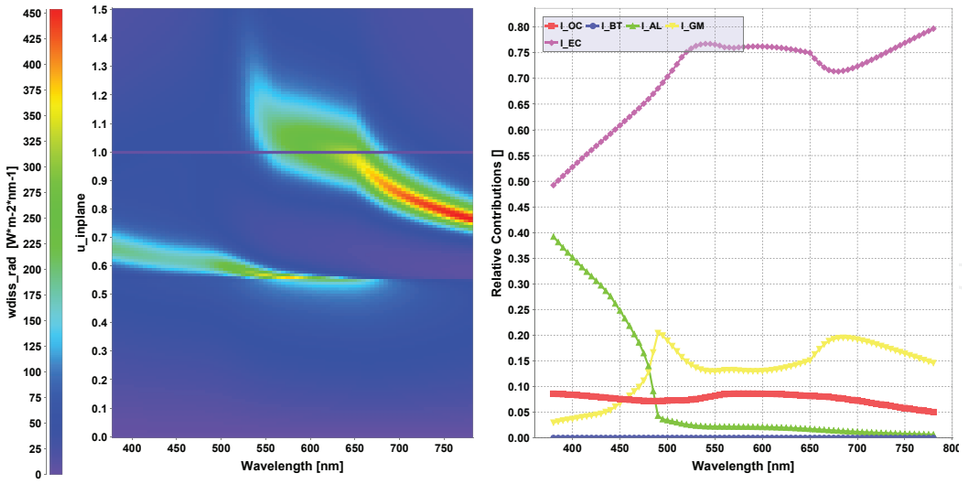

Fig. 12. Dipole emission calculation for the guest excitons in EML1. The dissipated power (left) and the mode analysis (right) are shown.

ITO being the negative electrode. A 10 ps laser pulse at 337 nm wavelength with energy of $1\mu J$ per square meter was used to generate a sheet of free carriers at the ITO-Alq_3-interface. The light intensity was kept sufficiently low to avoid space charge effects. Assuming HOMO and LUMO levels for the organic compound to be 5.6 and 3.0 eV, respectively, the two electrodes were acting as non-injecting layers because of their workfunctions of 5.0 eV for ITO and 4.1 eV for Al. For completeness, the (vanishing) injection was considered as thermionic and modeled after Scott and Malliaras (Scott & Malliaras, 1999).

Despite the energetic disorder of the transport states in organic compounds, the analysis was performed assuming Poole-Frenkel, field-dependent mobility, see Equation 10. The study of the impact of the energetic disorder on the current transient is beyond the goal of this text and it is known that the disorder does not affect the dispersive characteristics of TOF-related current signals (Bässler, 1993). Trapped charge carriers on sharp energy levels were described by Staudigel et al. (Staudigel et al, 1999) by a rate equation for trapped electrons n_t that reads

$$\frac{dn_t(x)}{dt} = \mu(E + \frac{kT}{ed_m})\sigma_t[n(N_t - n_t) - n_t N_0 e^{-\frac{E_{t_n}}{kT}}]. \tag{26}$$

In Equation (26), N_0 is the total number of available sites per unit volume, N_t is the trap concentration, E is the (local) electric field while E_{t_n} is the trap energy depth. Further, $d_m = N_t^{-1/3}$ is the mean trap distance and $\sigma_t = 5d_m^2$ is the effective capture cross section while n is the concentration of free carriers. Note, that Equation 26 is connected to Equation 4 by the relation $r_c = \mu E \sigma_t$ and $r_e = cN_0 e^{-\frac{E_{t_n}}{kT}}$. The electrical parameters for the modeled compound are summarized in Table 2. All calculations were performed with SETFOS (Fluxim AG, 2010). In Figure 13 we present the results for calculations considering no traps, shallow and deep traps.

When no traps are considered, a non-dispersive charge behavior is clearly recognized in the current transient. Contrarily, when deep traps (typically $E_{t_n} > 0.3$ eV at room temperature) are taken into account, the transient characteristics is evidently dispersive since no definite current drop is recognizable when the free electrons reach the aluminium electrode. A more careful analysis is needed in case of shallow traps ($E_{t_n} < 0.25$ eV at room temperature). Due to the relatively low energy barrier, trapped electrons are quickly released into the conduction

	n	p
μ_0	2.9e-9 cm^ 2/Vs	1e-8 cm^ 2/Vs
γ	7.3e-3 cm^ 0.5/V^ 0.5	0
LUMO/HOMO	3.0 eV	5.6 eV
E_{t_n}	−/0.212/0.33 eV	−

Table 2. Assumed electrical parameters for Alq_3 to reproduce the measurements presented in reference (Malliaras et al., 2001). Three different electron trapping depths, E_{t_n} were considered.

band. The resulting current transient characteristics shows an evident drop as the charges reach the aluminium electrode. Such “quasi-non-dispersive" behavior is often confused with trap-free characteristics (Malliaras et al., 2001), whereas trap states are still present but do not significantly damp the dynamics of the charges.

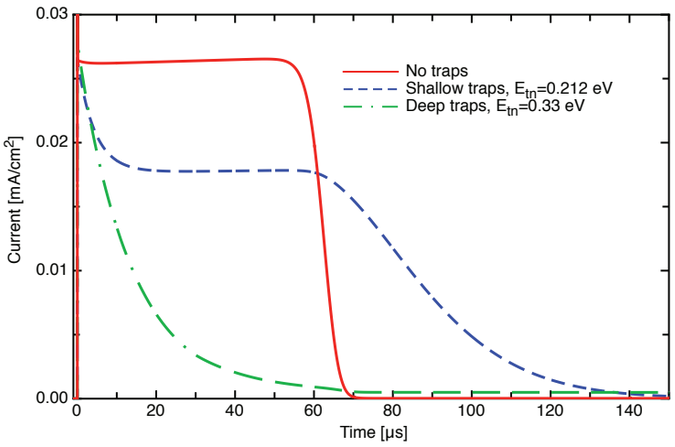

Fig. 13. Current transient characteristics of TOF measurements for samples with no traps (red solid line), shallow traps (blue dashed line) and deep traps (green dot-dashed line). As expected, trap-free compounds show a non-dispersive charge transport and charges in materials with deep traps exhibit a dispersive behavior. Weakly trapped charges on the contrary would indicate a non-dispersive behavior which is often mistakenly confused with the absence of traps (blue dashed line).

The behavior of the electrons in presence of deep or shallow traps can be analyzed looking at the charge density profiles for different times. Immediately after the light pulse that generates the charges a package of free electrons moves away from the ITO layer toward the positively charged aluminium electrode.
In Figure 14, left, we show the profiles of the charges in presence of deep traps, 10 μs after the light pulse. We recognize a symmetric, free electron packet partially overlapping the profile of the trapped electrons. When the free charges reach the aluminium electrode after 60 μs, their number is strongly reduced due to the many trapped states occupied during the flight from one electrode to the other (Figure 14, right). For the trapped electrons, it is energetically unfavorable to release back into a conductive state. They need many hundreds of microseconds to be de-trapped.

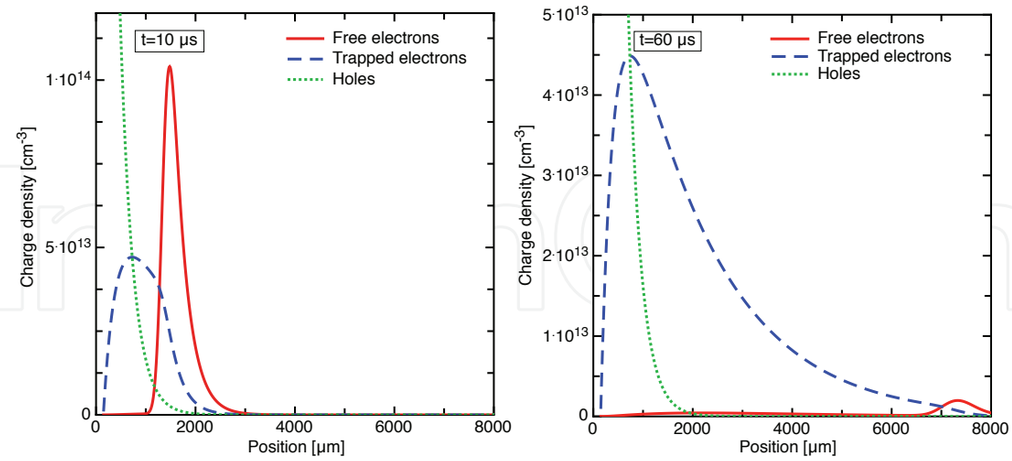

Fig. 14. *Deep traps.* Left: At $t = 10$ μs, the sharp packet of free electrons (red solid line) leaves the ITO electrode at position 0 μm and moves toward the aluminium electrode placed at position 8000 μm. A certain amount of charges remains trapped close to the ITO electrode (blue dashed line). Right: After 60 μs, those few free carriers that have not been trapped reach the aluminium electrode. Notice that trapped charges were "left behind" by the traveling free charge packet and did not move from their original position. Few trapped charges that begin to release back into the conduction band are recognizable through the slight increase of the free charges concentration around 2000 μm.

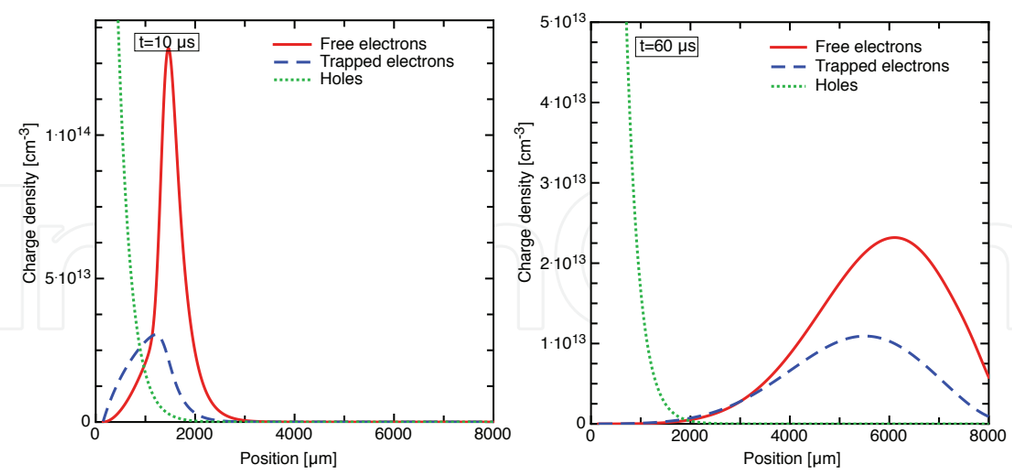

Fig. 15. *Shallow traps.* Left: Already at $t = 10$ μs, the free charge packet (red solid line) appears asymmetric due to the release of the weakly trapped charges (blue dashed line) around 1000 μm. Right: After 60 μs, a significant amount of free charges reaches the aluminium electrode. The fast kinetics of the trapped states makes them release back into the conduction band fast enough to follow the movement of the free electrons.

In Figure 15, left, we show the profiles of the charges in presence of shallow traps, 10 μs after the light pulse. The profile of the free electrons appears asymmetric because of the on-going release process of the temporarily trapped electrons. The kinetics of the trapped charges is so fast that the trapped packet follows the free electron packet in its travel toward the positive electrode. In Figure 15, right, we show the charge profiles at the moment they reach the aluminium electrode after 60 μs: the broad free electron packet overlaps the trapped charge packet so that both types appear to be extracted about at the same time. This explains the non-dispersive-like characteristics of the current transient in case of trapped states that are less than 25 meV below the LUMO level (blue dashed curve in Figure 13).
Despite the lack of precise information on the experimental procedure, the calculated current transients reproduce both qualitatively and quantitatively the measured curves presented by Malliaras et al.(Malliaras et al., 2001). Through our comprehensive numerical investigation, we could show that a qualitative analysis of the shape of the current transient is not enough to characterize trap-free samples. As a matter of facts, weakly trapped charges are able to follow the “flight" of free electrons through the device. Underestimating the presence of traps might lead a.o. to wrong statements on the lifetime of the device.

4. Parameter extraction

The following section introduces some aspects of parameter extraction in organic light-emitting devices (OLEDs). Two main applications are discussed. The first application is the extraction of the emission profile in a light-emitting layer of an OLED by a numerical method. The emission profile describes mathematically how the excitons are distributed inside the emissive layer. The numerical method presented is a linear least-square fit algorithm. The theory of numerical algorithms to extract the emission profile and some applications are also presented in more detail in Perucco et al. (Perucco et al, 2010). The second application is the extraction of EGDM parameters from multiple measured current-voltage curves by a nonlinear least-square algorithm.

4.1 Extraction of emission profiles in OLEDs

The objective of this section is to present and test a numerical fitting algorithm for the extraction of the emission profile and intrinsic source spectrum. The fitting algorithm is evaluated by adequate examples and validated on the basis of consistency checks. This is achieved by an optical model, where a transfer-matrix theory approach for multi-layer systems is used in combination with a dipole emission model. The optical model is implemented in the semiconducting emissive thin film optics simulator (SETFOS) (Fluxim AG, 2010). With SETFOS, the emission spectrum of an OLED based on an assumed emission profile and a known source spectrum is generated. The fitting method is then applied to the calculated emission spectra in order to estimate the emission profile and source spectrum. The comparison between the obtained and assumed emission profile and source spectrum is an indication of how successfully the inverse problem can be solved. Sections 4.1.1 deals with the mathematical derivation of this numerical fitting algorithm. In Section 4.1.2, the applications or consistency checks are presented.

4.1.1 Theory

The theoretical background of the fitting method is introduced in this section. The method is linear in terms how the measured emission spectrum is related to the unknown emission profile. For simplicity the mathematical formulation for the least-square problem is derived

for only one emitter. The emitter is characterized by the emission profile. For the moment, it is also assumed that the emission spectrum is measured in normal direction and therefore the light is unpolarized. In Section 4.1.1.1, this approach is extended further to multiple emitters described by several emission profiles and emission spectra measured for several angles θ. The extracted emission profile $P_e(\delta_j)$ is discretized at N relative positions $\delta_j = d_j/L$ in the light-emitting layer, where d_j is expressed as an absolute position and L is the width of the layer. The emission spectrum is divided into M wavelengths λ_i ($i = 1...M$). The fitted emission spectrum $I_f(\lambda_i)$ can be written as

$$I_f(\lambda_i) = \sum_{j=1}^{N} I_c(\lambda_i, \delta_j) \cdot P_e(\delta_j)\,, \tag{27}$$

where $I_c(\lambda_i, \delta_j)$ is the emission intensity for the wavelength λ_i and assuming a discrete emission profile (dirac function) at the relative position δ_j in the layer. The emission intensity is given by

$$I_c(\lambda_i, \delta_j) = I(\lambda_i, \delta_j) \cdot S(\lambda_i)\,, \tag{28}$$

where $I(\lambda_i, \delta_j)$ is the emission intensity for emissive dipoles with spectrally constant intensity. $S(\lambda_i)$ is the source spectrum. Between the measured emission spectrum $I_m(\lambda_i)$ and fitted emission spectrum $I_f(\lambda_i)$, a residuum can be defined and written as

$$r_1(\lambda_i) = I_f(\lambda_i) - I_m(\lambda_i)\,. \tag{29}$$

Equation 29 can be interpreted as a linear least-square problem, written as a system of linear equations

$$r_1(\lambda_i) = \sum_{j=1}^{N} I_c(\lambda_i, \delta_j) \cdot P_e(\delta_j) - I_m(\lambda_i)\,. \tag{30}$$

The system of equations is normally overdetermined (i.e. $M > N$) and thus is ill-posed. In matrix notation, the problem can be formulated as $r_1 = A \cdot x_1 - b_1$. The matrix A has the following structure

$$A = \begin{pmatrix} I_c(\lambda_1, \delta_1) & I_c(\lambda_1, \delta_2) & ... & I_c(\lambda_1, \delta_N) \\ I_c(\lambda_2, \delta_1) & I_c(\lambda_2, \delta_2) & ... & I_c(\lambda_2, \delta_N) \\ ... & ... & ... & ... \\ I_c(\lambda_M, \delta_1) & I_c(\lambda_M, \delta_2) & ... & I_c(\lambda_M, \delta_N) \end{pmatrix}, \tag{31}$$

b_1 is a vector containing the measured emission spectrum $I_m(\lambda_i)$ and the vector x_1 corresponds to the a priori unknown emission profile $P_e(\delta_j)$. The term linear refers to the linear combination between the matrix A and the vector x_1 of unknown weights. In every column of the matrix A, an emission spectrum is calculated for a dirac shaped emission profile at the position δ_j. The emission profile $P_e(\delta_j)$ at the relative position δ_j is the weight of the corresponding spectrum, respectively the column. The mathematical task is to minimize the length of the vector $\| r_1 \|$.

4.1.1.1 Extracting multiple emission profiles

The most general case of the emission spectrum is determined by the emission profile of multiple emitters $P_e(\delta_j^k)$ and emission angles θ_l. Given is the emission spectrum measured at O different angles ($l = 1...O$) and the OLED consists of Q different emitters ($k = 1...Q$) in

the same or in separate layers. The relation stated in Equation 27, combined with the definition of the residuum in Equation 30, can be extended to

$$r_2^{s,p}(\lambda_i, \theta_l) = \sum_{j=1}^{N} I_c^{s,p}(\lambda_i, \delta_j^k, \theta_l) \cdot P_e(\delta_j^k) - I_m^{s,p}(\lambda_i, \theta_l)\,. \tag{32}$$

$I_c^{s,p}(\lambda_i, \delta_j^k, \theta_l)$ stands for the s-polarized or p-polarized emission intensity at the wavelength λ_i. We assume a dirac shaped emission profile at the relative position δ_j^k for emitter k and an emission angle of θ_l. $P_e(\delta_j^k)$ is the emission profile at relative position δ_j for emitter k. Equation 32 represents a system of linear equations $r_2^{s,p} = A^{s,p} \cdot x_2 - b_2^{s,p}$, where the matrix $A^{s,p}$ contains the s-polarized and p-polarized emission spectra, the vector x_2 contains the information of several emission profiles and the vector $b_2^{s,p}$ represents the measured emission spectrum. The mathematical task is again to minimize the length of the vector $\parallel r_2^{s,p} \parallel$.

4.1.1.2 Extracting the intrinsic source spectrum

In the case of a single emitter, van Mensfoort et al. (Mensfoort et al., 2010) presented a method to extract the source spectrum of the light-emitting material. The source spectrum can be obtained by replacing the emission intensity $I_c^{s,p}(\lambda_i, \delta_j^k, \theta_l)$ by the emission intensity for emissive dipoles with spectrally constant intensity $I^{s,p}(\lambda_i, \delta_j^k, \theta_l)$ in Equation 32. This method is employed and evaluated in Section 4.1.2.2.

4.1.2 Applications

In this section, the reliability and limitation of the linear fitting method is addressed after it was mathematically deduced and described in Section 4.1.1. A given intrinsic source spectrum from a light-emitting material is assumed, together with an emission profile, stating where the dipoles are located in the device. The effects of quenching are disregarded in the presented applications below. First, quenching would likely limit the amount of dipoles close to the electrodes as the lifetime is very short. And secondly, light emitted from the dipoles is also captured in evanescent modes and therefore, does not couple out into air. Finally, the emission spectrum is generated by an optical dipole model described by Novotny (Novotny, 1997) and implemented in the simulator SETFOS (Fluxim AG, 2010). The calculated emission spectrum is used to solve the least-square problem in Equation 32. This allows the extraction of both, source spectrum and emission profile. The comparison of the extracted and assumed emission profile reveals the reliability of the presented algorithm. Throughout this text, an open cavity is used for the consistency checks. But the method here may also be applied to cavity and small-molecule based OLEDs. The OLED investigated here has a broad light-emitting polymer (LEP) of 100 nm. Further, the light-emitting layer is embedded between a 80 nm thick PEDOT:PSS anode and an aluminum cathode of 100 nm. The device is depicted in Figure 16. With respect to an experimental setup, the diameter of the semi-sphere glass lens is at least an order of magnitude larger than the diameter of the OLED. In order to achieve an absolute quantity of the emission intensity and emission profile, the assumed current density in all considered consistency checks is 10 mA/cm^2.

4.1.2.1 Extraction of the emission profile from angularly resolved emission spectra

As an introductory example, this section shows the application to angularly resolved emission intensity spectra. It compares the extracted emission profile from these spectra to an emission

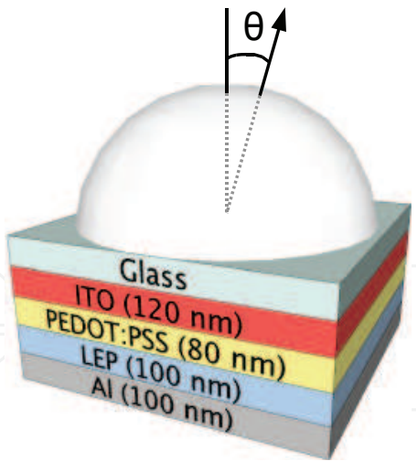

Fig. 16. OLED used to perform the parameter extraction tests with the semi-sphere glass lens. θ stands for the observation angle.

profile extracted from an emission intensity spectrum measured at normal angle. The assumed emission profile is Gaussian shaped, where the peak is set to 0.3 expressed in terms of a relative position in the emission layer. The width of the Gaussian shape is 20 nm.

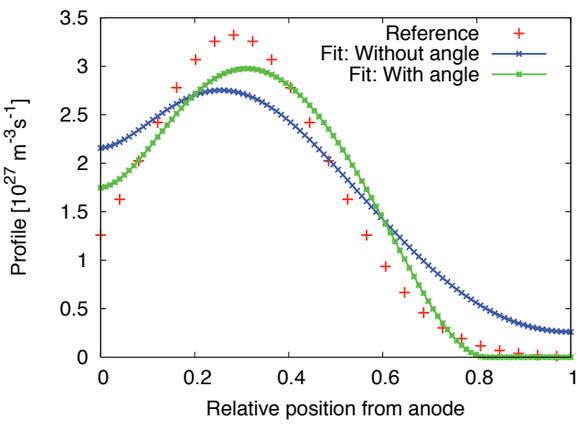

Fig. 17. Comparison between the assumed and extracted emission profiles. The emission profiles were extracted using angularly resolved emission spectra and an emission spectra measured at normal angle.

The comparison between the extracted and assumed emission profiles in Figure 17 shows an improvement of the extracted emission profile when angularly resolved emission intensity spectra are used. The fitted emission intensity spectra match visually perfectly the emission spectra serving as a measurement, as seen from Figure 18.

4.1.2.2 Source spectrum extraction

This section demonstrates the ability of the least-square algorithm to extract the intrinsic source spectrum of a light-emitting material. The same assumptions regarding the parameters of the emission profile are made as in Section 4.1.2.1. The extracted emission profile and source spectrum can be found on the left, respectively on the right in Figure 19.
It can be seen from Figure 19 that the source spectrum can be extracted very accurately. The emission profile is also well extracted and even the peak position is reproduced well.

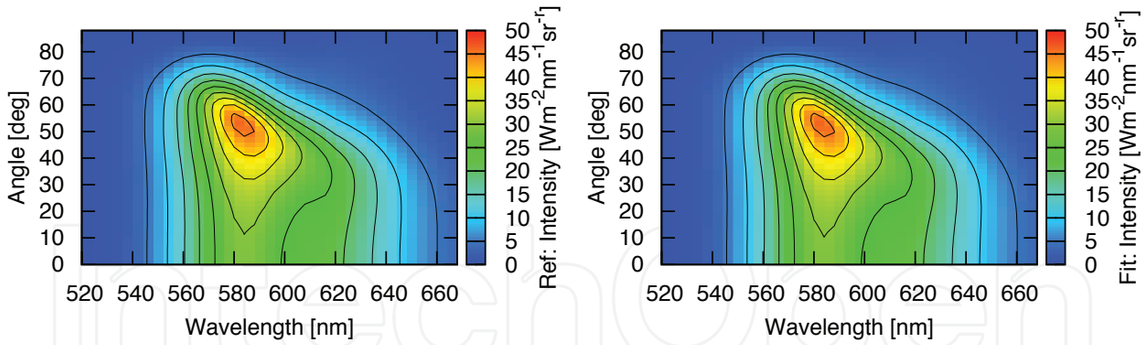

Fig. 18. Left: Angularly resolved emission intensity spectra serving as a measurement. Right: Fitted emission intensity spectra by the linear least-square algorithm.

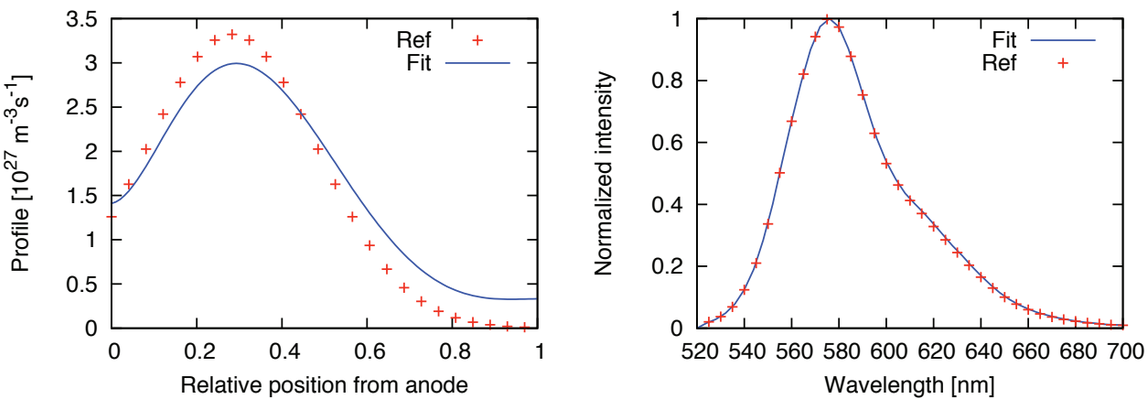

Fig. 19. Left: Comparison between the assumed and extracted emission profile. Right: Relation between the assumed and extracted intrinsic source spectrum by the method discussed in Section 4.1.1.2.

Illustrated in Figure 20 is the comparison between the assumed and fitted emission spectra, which are visually also in perfect agreement.

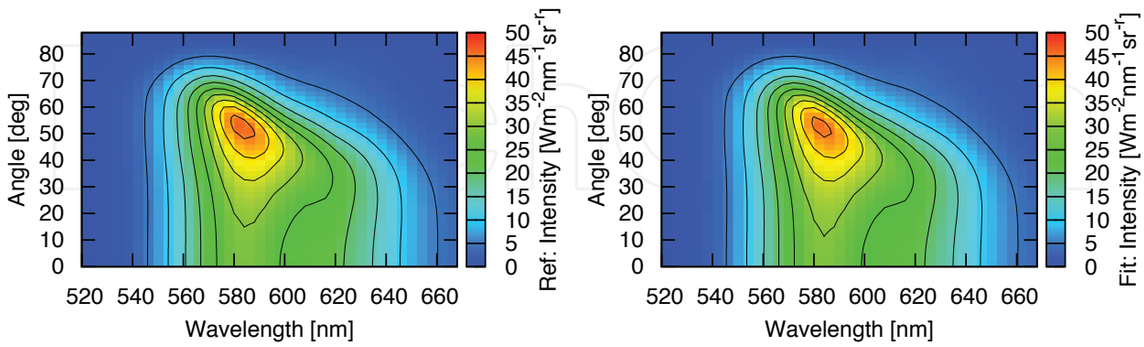

Fig. 20. Left: Angularly resolved emission intensity spectra serving as a measurement to extract the intrinsic source spectrum from. Right: Fitted emission intensity spectra by the linear least-square algorithm.

4.1.2.3 Extracting multiple emission profiles

Equation 32 explains how multiple emission profiles can be extracted from a measured emission intensity spectrum. This section illustrates the application of the method to a multi-emitter OLED. In this example, two emission profiles are extracted. The first assumed emission profile is Gaussian shaped with a peak at 0.7 and a width of 40 nm. The second assumed emission profile is also gaussian shaped, where the peak is at 0.3 and the width is 20 nm. Figure 21 shows the extracted and assumed emission profiles, as well as the reference and fitted emission intensity spectra.

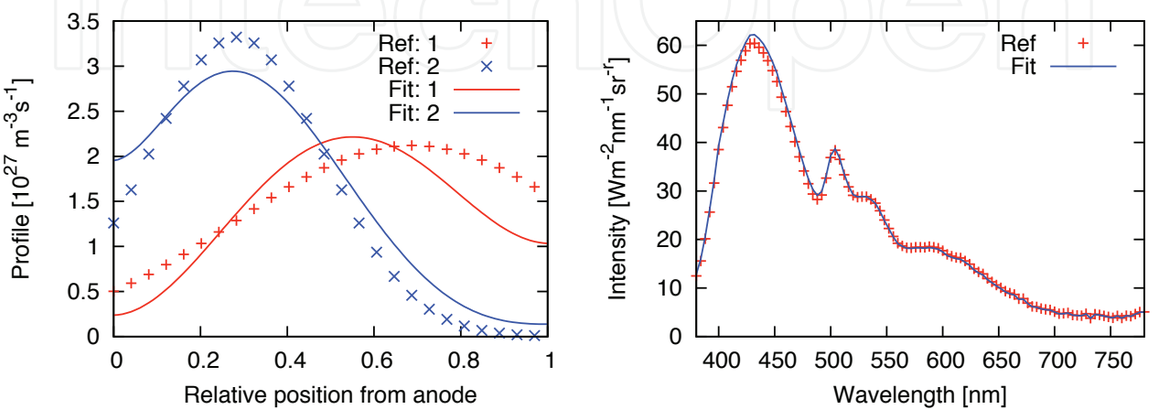

Fig. 21. Left: Showing the differences between the emission profiles from a multi-emitter OLED. The dotted curves represent the assumed emission profiles, whereas the lines stand for the extracted emission profiles. Right: Comparison between the measured and fitted emission intensity spectra.

Despite the fact that the assumed and fitted emission spectra match very well, some differences in the emission profiles are visible. Nonetheless, the general trend is explained by the extraction. For the second emission profile, both peak and width can be reproduced more or less. For the first emission profile, the flat emission profile can be explained as well.

4.2 Extraction of transport parameters from current-voltage curves

The following section deals with the application of a nonlinear least-square fitting algorithm to extract EGDM parameters from measured current-voltage curves. The nonlinear fitting algorithm, as well as the EDGM model is implemented in SETFOS. SETFOS is used to generate three hypothetical measured current-voltage curves at temperatures 320 K, 300 K and 280 K. All three current-voltage curves are simultaneously fitted for extracting the parameters. The device considered is a single-layer, hole-only device where the electrical layer has a thickness of 121.5 nm and the build-in voltage is 1.9 V. The energy diagram of the simulation device is depicted schematically in Figure 22. The following parameters are of interest: the mobility μ_p, the width of the Gaussian DOS σ_p, the density of chargeable sites N_0 and the workfunction at the cathode Φ_c. Meanwhile, the workfunction at the anode is held constant. The parameters represent real EGDM parameters as discussed in van Mensfoort et al. (Mensfoort et al., 2008b). The following parameters are assumed: $\mu_p = 1 \cdot 10^{-7}\, m^2/Vs$, $\sigma_p = 0.13\, eV$, $N_0 = 6 \cdot 10^{26}\, 1/m^3$ and $\Phi_c = 3.2\, eV$. The mobility μ_p is related to Equation 11 in the following way: $\mu_0(T) = \mu_p \exp\left(-0.39(\sigma/(kT))^2\right)$. The left hand side of Figure 23 shows that the nonlinear least-square algorithm is capable of extracting all four EGDM parameters as the current-voltage curves at the same temperature match each other visually perfectly.

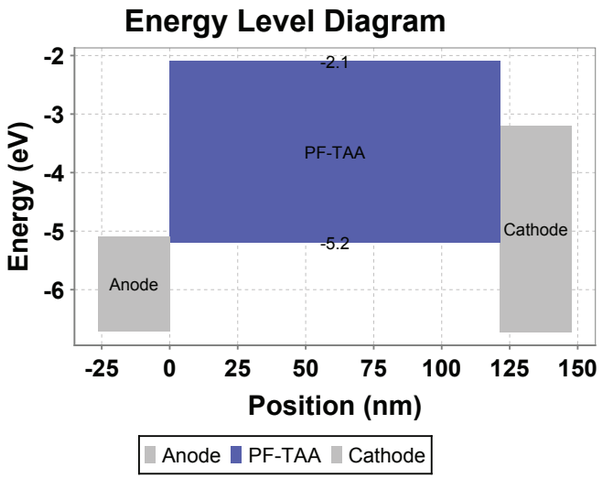

Fig. 22. Energy diagram for the simulated device. The workfunction at the anode side is held constant at 5.1 eV, while the workfunction at the cathode side Φ_c is being optimized. The HOMO and LUMO levels are 5.2 eV, respectively 2.1 eV.

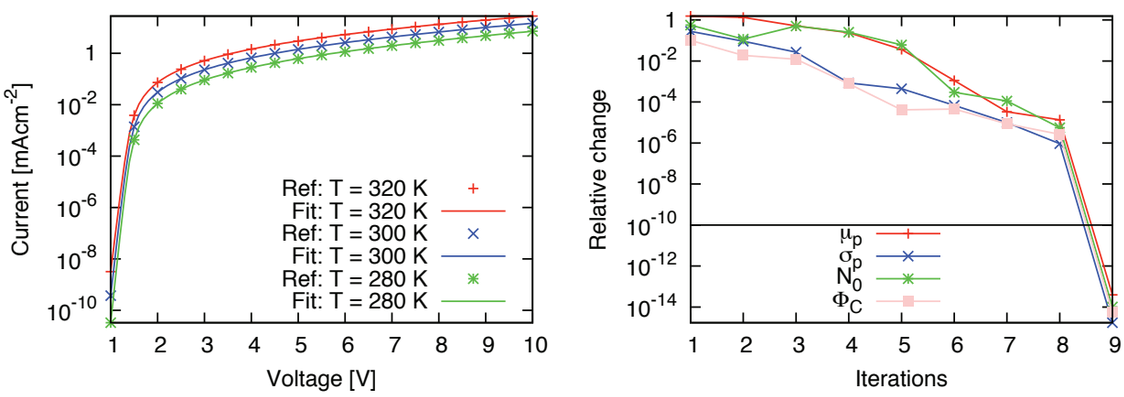

Fig. 23. Left: Comparison between the measured current-voltage curves (points) and the fitted current-voltage curves (lines). The extraction of parameters is done using all three measured curves at different temperatures at the same time in order to get more accurate results. Right: Showing the relative change in the parameters as a function of iterations. The black line represents the relative change which must be achieved as a termination criterion.

The right hand side of Figure 23 illustrates the relative error of the EGDM parameters as a function of the optimization iteration. The relative change is defined as $(p_{i+1} - p_i)/p_{i+1}$, where p_i is the value of parameter p at iteration i. The black line shows the relative change, which must be achieved in order to terminate the optimization process. All four parameters obtained after 9 iterations have a smaller relative change than 10^{-10}. Depending on the parameter, it can be seen from Figure 23 that the relative change in the parameter is initially between 10^{-1} and 1. The assumed, extracted and initial parameters for the fit can be seen in Table 3.

Table 3 shows that the nonlinear least-square algorithm is able to accurately extract the assumed EGDM parameters. A potential limitation of the nonlinear least-square method is that the error landscape should be smooth and the initial parameters should not be too far off from the assumed values, otherwise the method might converge into another local minimum.

Parameter	Assumed	Extracted	Initial
μ_p $[10^{-7}\ m^2/Vs]$	1.400	1.398	3.000
σ_p $[eV]$	0.130	0.130	0.100
N_0 $[10^{26}\ 1/m^3]$	6.000	5.984	1.000
Φ_c $[eV]$	3.200	3.200	3.200

Table 3. Assumed and extracted EGDM mobility model parameters for the test, as well as initial parameters for the nonlinear least-square algorithm.

For such situations and to cross-check the fit result, potentially more time-consuming global optimization routines may be used (Fluxim AG, 2010).
In a post-processing step, the correlation coefficients for the four model parameters can be calculated at the best fit point. These coefficients corresponding to the fit result listed in Table 3 are shown in Table 4.

	μ_p	σ_p	N_0	Φ_c
μ_p	1.00	0.94	0.39	-0.95
σ_p		1.00	0.07	-0.84
N_0			1.00	-0.55
Φ_c				1.00

Table 4. Correlation coefficients for the EGDM parameters at the best fit point in case of a multiple current-voltage curve fit as seen in Figure 23: mobility μ_p, width of Gaussian DOS σ_p, density of chargeable sites N_0 and workfunction cathode Φ_c

A correlation of 0 indicates no correlation between the two parameters, meaning the parameters are independent from each other. Whereas a correlation of -1 or 1 means perfect correlation. A slight change in the same direction on the fitted curve can be achieved by either parameter. As an example we consider the high correlation of -0.95 between the hole mobility μ_p and the workfunction ϕ_c. This means that the current can be increased by either increasing the mobility μ_p or lowering the workfunction ϕ_c. Such correlations do physically make sense, however they can complicate parameter fitting. Overall, our electrical parameter extraction example demonstrates, that rather complex physical models can be fitted to current-voltage curves thus making an efficient numerical analysis of measured data suitable.

5. Conclusions

We have given an overview on state-of-the-art electronic and optical device models for OLEDs. We demonstrated that numerical models are able to simulate different kinds of measurement setups for OLED characterization. We investigate the influence of the EGDM and the Gaussian density of states on the current-voltage curves, the dark-injection transients and the frequency response for a polymer device. All three characterization curves change significantly, if the disorder model ingredients are taken into account. The simulation results were successfully compared with analytical solutions, where applicable. We also show that the physical models can be combined with a nonlinear least-square fitting algorithm for extracting emission profiles and charge transport parameters from (hypothetical) measurements. In terms of optical device characteristics, quantitative outcoupling mode contributions and angular characteristics are presented as well as results of an emission zone extraction method. Simulations of electronic and optical processees in

a doped, multilayer OLED are also presented, thus highlighting, that comprehensive OLED device simulations are becoming feasible.

6. Acknowledgement

We acknowledge financial support from the European Community's Seventh Research Framework program for the AEVIOM.eu project under grant agreement no. 213708.

7. References

Bässler H., "*Charge Transport in Disordered Organic Photoconductors a Monte Carlo Simulation Study*," Phys. Status Solidy B **175**, 1 (1993).

Blom P. W. M., de Jong M. J. M., and Vleggaar J. J. M., "*Electron and hole transport in poly(p-phenylene vinylene) devices*," Appl. Phys. Lett. 68, 3308 (1996).

Chance R. R., Prock A., Silbey R., "*Molecular Fluorescence and Energy Transfer Near Interfaces*," Advances in Chemical Physics, Vol. 37, John Wiley and Sons, pp. 16 (1978).

Crone B. K, Davids P. S, Campbell I. H, and Smith D. L., "*Device model investigation of bilayer organic light emitting diodes*," J. Appl. Phys. 87, 1974 (2000).

Dexter D. L., "*Theory of Sensitized Luminescence in Solids*," J. Chem. Phys. 21 (5), 836 (1953).

Fluxim AG, "*Semiconducting thin film optics simulator SETFOS*," Website: http://www.fluxim.com.

Förster T., "*Zwischenmolekulare Energiewanderung und Fluoreszenz*," Ann. Phys. 6 (2), 55-75 (1948).

Helfrich W. and Mark P., "*Raumladungsbeschränkte Ströme in Anthrazen als Mittel zur Bestimmung der Beweglichkeit von Defektelektronen*," Z. Phys. **166**, 370 (1962).

Knapp E., Häusermann R., Schwarzenbach H. U., Ruhstaller B., "*Numerical simulation of charge transport in disordered organic semiconductor devices*," J. Appl. Phys. 108, 054504 (2010).

Langevin P., Ann. Chim. Phys. VII **28**, 433 (1903).

Malliaras G. G., Shen Y., Dunlap D. H., Murata H. and Kafafi Z. H., "*Nondispersive electron transport transport in Alq_3*,", Appl. Phys. Lett. **79**, 16 (2001).

Mott N. P. and Gurney R. W., "*Electronic Processes in Ionic Crystals*," Oxford Univ. Press, London (1938).

Novotny L., "*Allowed and forbidden light in near-field optics. I. A single dipolar light source*," J. Opt. Soc. Am. A 14, 91 (1997).

Pasveer W. F., Cottaar J., Tanase C., Coehoorn R., Bobbert P. A., Blom P. W. M. et al., "*Unified description of charge-carrier mobilities in disordered semiconducting polymers*," Phys. Rev. Lett. **94**, 206601 (2005).

Pautmeier L., Richert R., and Bässler H., Synth. Metals 37, 271 (1990).

Perucco B., Reinke N. A., Müller F., Rezzonico D., and Ruhstaller B., "*The influence of the optical environment on the shape of the emission profile and methods of its determination*," Proc. SPIE 7722, 77220F (2010).

Perucco B., Reinke N. A., Rezzonico D., Moos M., and Ruhstaller B., "*Analysis of the emission profile in organic light-emitting devices*," Optics Express, Vol. 18, Issue S2, pp. A246-A260 (2010).

Preezant Y., Roichman Y., and Tessler N., "*Amorphous organic devices - degenerate semiconductors*," J. Phys. Cond. Matt. **14**, 9913 (2002).

Roichman Y. and Tessler N., "*Generalized Einstein relation for disordered semiconductors: implications for device performance*," Appl. Phys. Lett. **80**, 1948 (2002).

Ruhstaller B. et al., "*Simulating Electronic and Optical Processes in Multilayer Organic Light-Emitting Devices,*" IEEE J. Sel. Top. Quantum Electron. 9, 3 (2003).

Ruhstaller B. et al., "*Transient and steady-state behavior of space charges in multilayer organic light-emitting diodes,*" J. Appl. Phys. 89 (2001).

Scharfetter D. L. and Gummel H. K., "*Large-signal analysis of a silicon read diode oscillator,*" IEEE Trans. Electr. Dev. 16, 64 (1969).

Scott J. C. and Malliaras G. G, "*Charge injection and recombination at the metalâĂŞorganic interface,*" Chem. Phys. Lett. 299, 115 (1999).

Shao J., Wright G. T., "*Characteristics of the space-charge-limited dieletric diode at very high frequencies,*" Solid-State Electron. 3, 291 (1961).

Staudigel J. et al., "*A quantitative numerical model of multilayer vapor-deposited organic light emitting diodes,*" J. of Appl. Phys. **86**, 7 (1999).

Tanase C., Meijer E. J., Blom P. W. M., and de Leeuw D., Phys. Rev. B 91, 4 (2003).

van Mensfoort S. L. M. and Coehoorn R., "*Effect of Gaussian disorder on the voltage dependence of the current density in sandwich-type devices based on organic semiconductors,*" Phys. Rev. B 78, 085207 (2008).

van Mensfoort S. L. M., Vulto S. I. E, Janssen R. A. J., and Coehoorn R., "*Hole transport in polyfluorene-based sandwich-type devices: Quantitative analysis of the role of energetic disorder,*" Phys. Rev. B, 78, 085208 (2008).

van Mensfoort S. L. M., Carvelli M., Megens M., Wehenkel D., Bartyzel M., Greiner H., Janssen R. A. J., and Coehoorn R., "*Measuring the emission profile in organic light-emitting diodes with nanometre resolution,*" Nature Photonics 4, 329-335 (2010).

Vissenberg M. C. J. M. and Matters M., Phys. Rev. B 57, 12964 (1998).

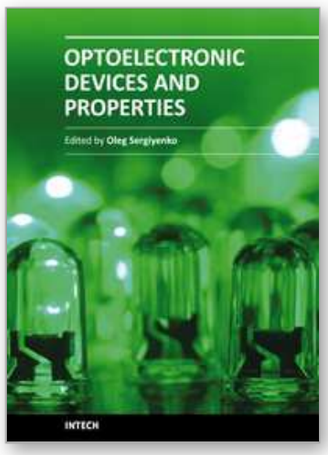

Optoelectronic Devices and Properties

Edited by Prof. Oleg Sergiyenko

ISBN 978-953-307-204-3
Hard cover, 660 pages
Publisher InTech
Published online 19, April, 2011
Published in print edition April, 2011

Optoelectronic devices impact many areas of society, from simple household appliances and multimedia systems to communications, computing, spatial scanning, optical monitoring, 3D measurements and medical instruments. This is the most complete book about optoelectromechanic systems and semiconductor optoelectronic devices; it provides an accessible, well-organized overview of optoelectronic devices and properties that emphasizes basic principles.

How to reference

In order to correctly reference this scholarly work, feel free to copy and paste the following:

Beat Ruhstaller, Evelyne Knapp, Benjamin Perucco, Nils Reinke, Daniele Rezzonico and Felix Müller (2011). Advanced Numerical Simulation of Organic Light-emitting Devices, Optoelectronic Devices and Properties, Prof. Oleg Sergiyenko (Ed.), ISBN: 978-953-307-204-3, InTech, Available from: http://www.intechopen.com/books/optoelectronic-devices-and-properties/advanced-numerical-simulation-of-organic-light-emitting-devices

INTECH
open science | open minds

InTech Europe
University Campus STeP Ri
Slavka Krautzeka 83/A
51000 Rijeka, Croatia
Phone: +385 (51) 770 447
Fax: +385 (51) 686 166
www.intechopen.com

InTech China
Unit 405, Office Block, Hotel Equatorial Shanghai
No.65, Yan An Road (West), Shanghai, 200040, China
中国上海市延安西路65号上海国际贵都大饭店办公楼405单元
Phone: +86-21-62489820
Fax: +86-21-62489821

IntechOpen